AGU PUBLICATIONS

JGR

Journal of Geophysical Research: Oceans

RESEARCH ARTICLE

10.1002/2016JC011844

Key Points:
- Prestack full-waveform inversion of multichannel seismic data for seismic oceanography
- Specifically designed data preconditioning for acoustic noise reduction
- Temperature and salinity models resolve with an accuracy of 0.18oC and 0.08 PSU, respectively, and a resolution of 70 m

Supporting Information:
- Supporting Information S1
- Figure S1
- Figure S2
- Figure S3
- Figure S4
- Figure S5
- Figure S6

Correspondence to:
D. Dagnino,
dagnino@icm.csic.es

Citation:
Dagnino, D., V. Sallarès, B. Biescas, and C. R. Ranero (2016), Fine-scale thermohaline ocean structure retrieved with 2-D prestack full-waveform inversion of multichannel seismic data: Application to the Gulf of Cadiz (SW Iberia), *J. Geophys. Res. Oceans*, *121*, 5452–5469, doi:10.1002/2016JC011844.

Received 30 MAR 2016
Accepted 27 JUN 2016
Accepted article online 29 JUN 2016
Published online 5 AUG 2016

Fine-scale thermohaline ocean structure retrieved with 2-D prestack full-waveform inversion of multichannel seismic data: Application to the Gulf of Cadiz (SW Iberia)

D. Dagnino[1], V. Sallarès[1], B. Biescas[2], and C. R. Ranero[3]

[1]Barcelona Center for Subsurface Imaging, Institute of Marine Sciences, CSIC, Barcelona, Spain, [2]Istituto di Scienze Marine - CNR, Bologna, Italy, [3]Barcelona Center for Subsurface Imaging, Institute of Marine Sciences, ICREA at CSIC, Barcelona, Spain

Abstract This work demonstrates the feasibility of 2-D time-domain, adjoint-state acoustic full-waveform inversion (FWI) to retrieve high-resolution models of ocean physical parameters such as sound speed, temperature and salinity. The proposed method is first described and then applied to prestack multichannel seismic (MCS) data acquired in the Gulf of Cadiz (SW Iberia) in 2007 in the framework of the Geophysical Oceanography project. The inversion strategy flow includes specifically designed data preconditioning for acoustic noise reduction, followed by the inversion of sound speed in the shotgather domain. We show that the final sound speed model has a horizontal resolution of $\sim$ 70 m, which is two orders of magnitude better than that of the initial model constructed with coincident eXpendable Bathy Thermograph (XBT) data, and close to the theoretical resolution of $O(\lambda)$. Temperature (T) and salinity (S) are retrieved with the same lateral resolution as sound speed by combining the inverted sound speed model with the thermodynamic equation of seawater and a local, depth-dependent T-S relation derived from regional conductivity-temperature-depth (CTD) measurements of the National Oceanic and Atmospheric Administration (NOAA) database. The comparison of the inverted T and S models with XBT and CTD casts deployed simultaneously to the MCS acquisition shows that the thermohaline contrasts are resolved with an accuracy of 0.18^{o}C for temperature and 0.08 PSU for salinity. The combination of oceanographic and MCS data into a common, pseudo-automatic inversion scheme allows to quantitatively resolve submeso-scale features that ought to be incorporated into larger-scale ocean models of oceans structure and circulation.

1. Introduction

Flow interaction generates many different oceanographic processes and features from the largest scales, where the energy is injected, to the smallest ones, where it is dissipated. The resulting structures display distinctive thermohaline signatures, which can be detected and imaged using dedicated oceanographic instrumentation such as XBT and CTD probes. The data provided by such systems typically have a resolution of O(1 m) in the vertical direction but - depending on the experiment design - only several kilometers in the horizontal one. The low lateral resolution of these conventional observational oceanographic systems has been a limiting factor to characterize and understand important oceanographic processes that occur at horizontal scales of $O(<10^3$ m), and particularly the transition from anisotropic internal wave motions to isotropic turbulence [e.g., *Thorpe*, 2005; *Müller et al*., 2005].

Following the seminal work of *Holbrook* [2003], several studies have shown that this observational gap can be covered with multichannel seismic (MCS) systems, which allow imaging the 2-D thermohaline structure along transects of tens to hundreds of kilometers with a horizontal resolution of a few tens of meters, to full ocean depth. The application of MCS to oceanography has been called seismic oceanography (SO). Most SO works performed to date have focused on processing the MCS data in order to create 2-D acoustic reflectivity maps of the thermohaline boundaries, and their interpretation is based on the direct or spectral analysis of the resulting acoustic reflectivity maps. Together, these studies have demonstrated the potential of MCS data to image various structures of oceanographic interest [e.g., *Biescas et al*., 2008; *Buffett et al*., 2009; *Eakin et al*., 2011; *Sheen et al*., 2009] and to provide information on internal wave dynamics and turbulence with unprecedented lateral detail [e.g., *Holbrook and Fer*, 2005; *Sheen et al*., 2009; *Krahmann et al*., 2008; *Sallarès et al*., 2016].

Additionally, the fact that MCS acquisition has been widely used for academic, and oil exploration geological studies for the past 50 years, makes that a large volume of potentially available data exists in most parts of the World's oceans that are still unexploited for oceanographic purposes.

Water reflectivity is generated at the boundaries between water masses showing contrasts of acoustic impedance. In particular, it mainly maps sound speed (V) through temperature (T) and salinity (S) gradients, with a relative contribution of ~5:1 [*Sallarès et al*., 2009]. Two main different procedures have been explored to extract V and/or T and S out from acoustic reflectivity. One strategy follows the original work of *Papenberg et al*. [2010] in the Gulf of Cadiz, which is based on the convolution model. The key steps of this technique are generating true-amplitude, time-migrated MCS sections and deconvolve the combined seismograms (i.e., the stacked seismic traces) with an estimated source wavelet to recover the reflection coefficients. To recover physical properties from the reflection coefficients two strategies have been followed: *Papenberg et al*. [2010] recovered V contrasts assuming constant density and then transformed V to T and S; *Biescas et al*. [2014], and *Huang et al*. [2011] calculated acoustic impedance from reflection coefficients and then calculated T, S and density. The sequence is repeated for each stacked seismic trace along the MCS profile to construct a 2-D section. As a second strategy, different full-waveform inversion (FWI)-based approaches have been proposed and tested. The common steps of FWI methods are computing the seismograms, calculating an objective function that measures differences between observed and simulated seismograms, calculating the gradient of the objective function with respect to the parameters of interest, and then minimizing it iteratively. The first application of FWI to the water layer was made by *Wood et al*. [2008], who successfully retrieved 1-D sound speed profiles. In this case, the individual seismograms are computed applying the plane-wave reflection transmission matrix, or reflectivity, method [*Kennett and Kerry*, 1979], which assumes laterally invariant models for each common mid-point (CMP) gather; whereas the partial derivatives with respect to V are calculated semi-analytically [*Dietrich and Kormendi*, 1990]. This technique, preceded by global inversion using a genetic algorithm to build the initial model, was also applied to series of CMPs to construct interpolated 2-D maps of V, T, and S along an MCS profile at the South China Sea by *Padhi et al*. [2015]. Alternatively, adjoint-state FWI [*Lailly*, 1983; *Tarantola*, 1984] has also been explored. The main differences of adjoint state-based with respect to reflectivity-based inversion are that in the first the full wavefield is simulated resolving the acoustic wave equation (i.e., no approximations are made); and that the gradients, or sensitivity kernels, of the parameters to be inverted, are computed numerically following the adjoint-state formulation. So far, adjoint-state FWI of the water layer has only been tested on 1-D synthetic data that simulate stacked seismic traces. In this case, it has been shown that assuming a perfectly processed, noise-free data containing unlimited low frequencies, and using a known source wavelet with homogeneous directivity, no phase-flipping at the water-air interface and perfect hydrophone measurements; it is possible to invert V and then derive T and S [*Kormann et al*., 2011], or to directly inverting T and S using the thermodynamic equation of seawater to derive the kernels of T and S from the kernels of V and density [*Bornstein et al*., 2013], with an accuracy of ~0.1°C and ~0.06 PSU, respectively. The potential problems to apply 2-D FWI to prestack field data recordings (i.e., the original shot-gather recordings instead of the stacked traces) are the high computational burden, the lack of appropriate initial models limited by the lowest frequencies present in the data, the imperfectly known source wavelet, and the extremely poor signal-to-noise ratio (SNR) of the individual traces.

Here we show that the 2-D adjoint-state FWI of water layer properties using prestack MCS data is actually feasible. We have developed a dedicated 2-D FWI code, a data processing sequence, and an inversion strategy, which are specific for water layer inversion; and we have applied them to MCS data acquired in the Gulf of Cadiz (SW Iberia). The proposed method has allowed retrieving 2-D V (with V contrasts of a few m/s), T and S maps across the Mediterranean undercurrent (MU) with lateral resolutions of ~70 m, and an accuracy of ~0.18°C and ~0.08 PSU. In the next sections, we first describe the data set and the oceanographic setting of the surveyed area; and then, we present the methodology developed and applied, including data processing, forward modelling, gradient calculation and preconditioning, source and parameters inversion, and objective function minimization. Finally, we describe our results and we compare them to probe-based oceanographic measures to quantify their lateral resolution and accuracy.

2. MCS Data Acquisition in the Gulf of Cadiz (SW Iberia)

The data set used in this work corresponds to an MCS profile acquired in the Gulf of Cadiz (SW Iberia) in 2007, in the framework of the EU-funded GO (Geophysical Oceanography) project (Figure 1). This region is

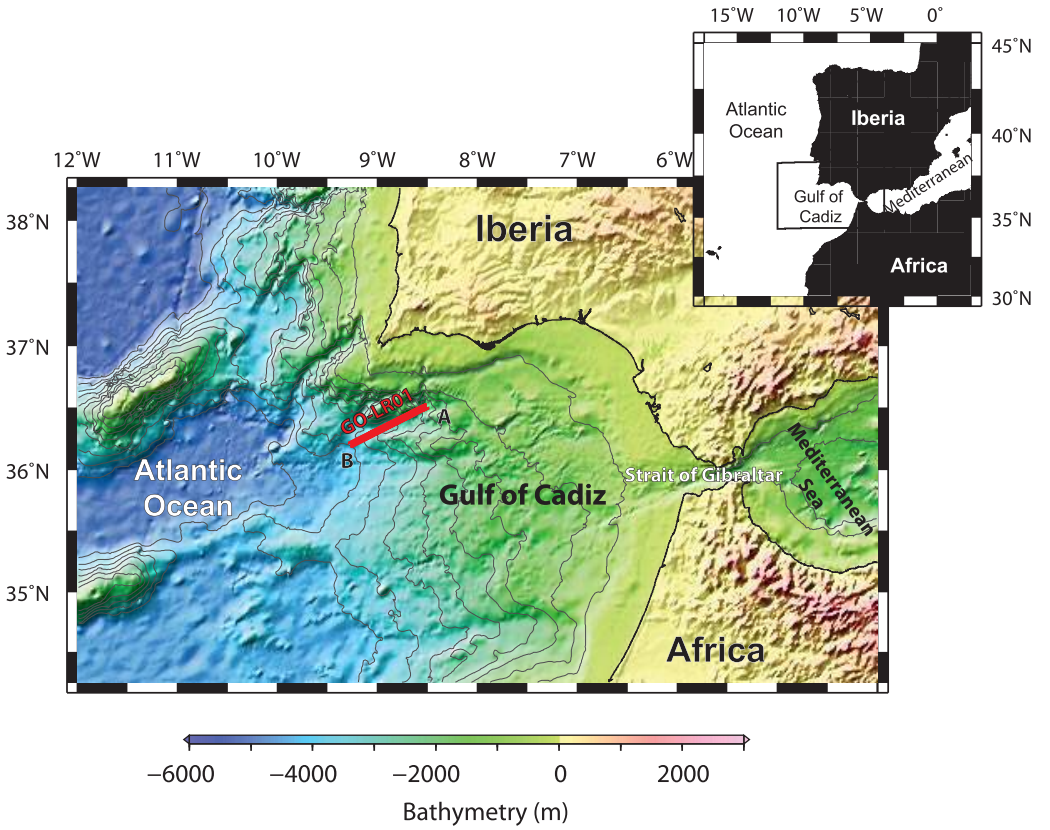

Figure 1. Location map showing the studied area located at the Gulf of Cadiz. We draw a red line to illustrate the part of the LR01 line we have used in the inversion. Label A and B indicate the initial and last shot, respectively.

characterized by the presence of the warm and salty Mediterranean outflow water, which crosses the Strait of Gibraltar and cascades down the continental slope following the bathymetric features of the South Iberian margin, until it reaches neutral buoyancy with respect to the surrounding Atlantic water at a depth of 700–1500 m. The dense overflow, also known as MU, is constituted by two cores [*Hobbs et al*., 2009], an upper one located at 700–800 m; and a lower one, centred at 1000–1200 m. The MU is deflected northward by the Coriolis force and follows the western Iberia continental slope at about this depth, becoming progressively diluted as it flows to the North [*Buffett et al*., 2009]. Additionally, a substantial part of the MU detaches from the seafloor at the approximate location of the Portimao canyon, feeding the internal Gulf of Cadiz and mixing with North Atlantic Intermediate Water and North Atlantic Deep Water [*Bower*, 2002; *Ambar et al*., 2002; *Buffett et al*., 2009]. The interaction of the MU with the complex topography that shapes the continental slope causes rotating lenses of Mediterranean water, or meddies, to separate from the core of the MU and get dispersed into the Atlantic [*Armi et al*., 1989; *Richardson et al*., 2000]. The entrainment of the Atlantic waters by the MU creates a complex thermohaline finestructure that can be imaged by differences in acoustic impedance [*Buffett et al*., 2009; *Song et al*., 2011]. The observed features include meddies [*Biescas et al*., 2008; *Papenberg et al*., 2010], double-diffusive thermohaline staircases at the bottom of the MU [*Tait and Howe*, 1968; *Ruddick*, 2003; *Biescas et al*., 2010], isopycnal stirring by mesoscale eddies, or diapycnal mixing [*Ferrari and Polzin*, 2005; *Biescas et al*., 2014].

The MCS data used in this work were acquired onboard the British RRS Discovery in May 2007 [*Hobbs et al*., 2007]. In particular, the inverted data are constituted by a total of 1107 shot-gathers recorded along a 55 km-long segment of the LR01 line, with an average shot spacing of 50.4 m. (Figure 1). The acoustic source was composed of 6 Bolt 1500LL airguns divided in two identical subarrays of 3 guns each with chamber sizes of 700, 300 and 160 cubic inches, which were towed at a depth of 8 m. According to tests made, the usable frequency band is 10–60 Hz. The pressure field was recorded by a 192 channels, 2.4 km-long, SERCEL SEAL streamer; with a group interval of 12.5 m. Each channel records the stacked signal of 16 hydrophones separated 0.625 m. The time sampling of the seismic records is 0.001 s. The distance from the centre

of the source to the first channel was 84 m, and the streamer was situated at a nominal depth of 8 m by 9 depth-controlling birds equally spaced along the streamer.

In the 50 km-long segment of the LR01 line, 22 lockheed Martin Sippican XBT-T5 were deployed simultaneously during the MCS acquisition with an approximate mean separation of 2.5 km. XBTs measured T and depth, where depth is calculated from the diving time and the diving speed. Sound speed is calculated from T and depth assuming a constant S.

3. Methodology

3.1. Data Processing

An essential step to perform prestack FWI of water layer data is reducing noise to increase SNR (Figure 2a). It must be noted that the sound speed contrasts associated with the oceans fine structure are of $\sim 1 - 5$ m/s. This means that maximum water reflectivity is 10^2–10^3 times weaker than that of geological boundaries in the solid Earth, whereas the ambient noise level is the same. The redundancy of multichannel systems is key to improve SNR and to obtain clear images of the subsurface reflectors. In the case of the GO experiment the maximum fold of the system is 24, so that we can sum the signal of up to 24 seismograms that illuminate the same point of the profile (or CMP) to construct the stacked image, which can then be interpreted and/or used to extract water properties. However, this strategy cannot be used in prestack FWI, because the data to be inverted are the original records of each of the 1107 shots at the 192 streamer channels (212,544 individual seismograms in total). Instead, we have designed a specific data processing flow to attenuate noise without modifying the recorded waveforms (both amplitudes and phases), which is essential to perform FWI. Another difference with respect to all previous studies is that we do not eliminate the direct wave travelling near the sea surface and we do not deconvolve the data. Instead, we incorporate an initial guess of the source wavelet in the first step of the wavefield modelling and we then invert for the actual source signature of each shot.

In summary, the processing flow designed and applied to the LR01 line consists of the following steps:

1. The recorded seismograms are multiplied by $\sqrt{t}$ to reduce the 3-D amplitude decay due the geometrical spreading. This correction factor allows to compare the synthetic data, generated with a 2-D acoustic solver, with the observed data, which are actually 3-D.

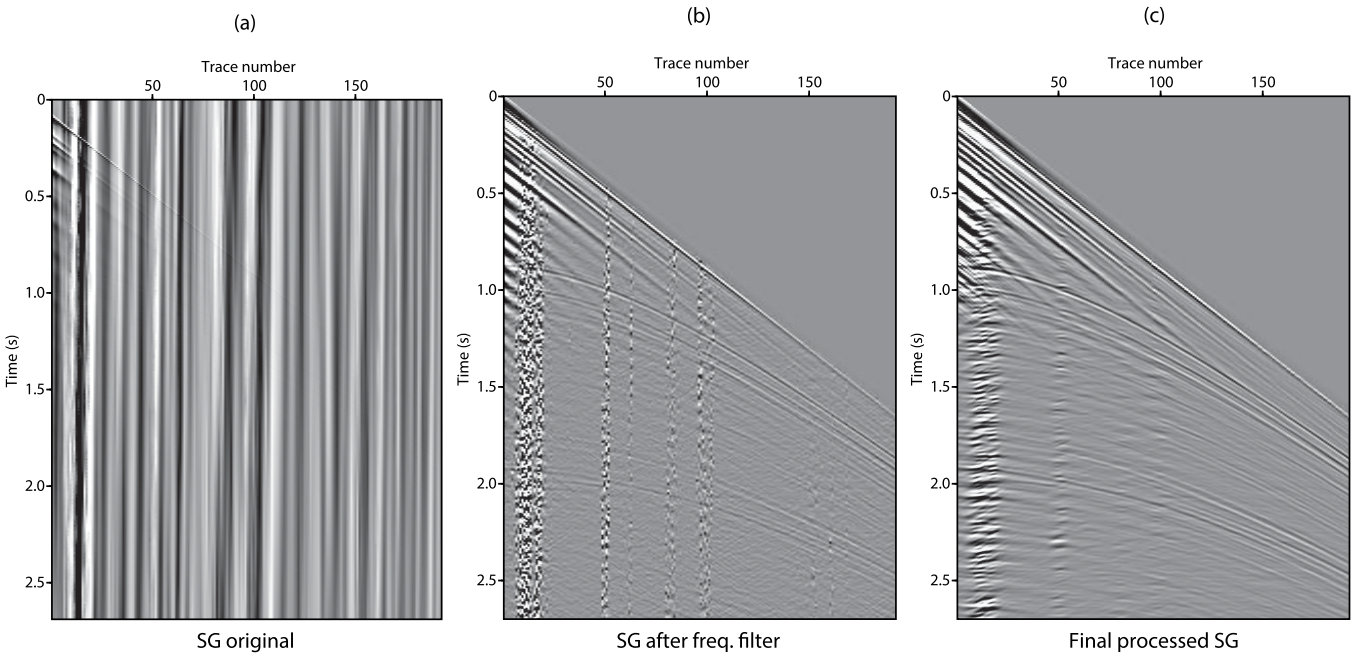

Figure 2. (a) Shot-gather before processing. (b) First shot-gather of the seismic line filter with a sixth-order band-pass zero-phase Butterworth filter. (c) Shot-gather (Figure 2a) after all the data processing.

2. Select records to a two-way-time of 2.7 s. This corresponds to a depth of ∼2000 *m*, which is our maximum target depth.
3. Apply a sixth-order band-pass Butterworth filter. The low-cut and high-cut frequency of the band-pass filter are 10 Hz and 60 Hz, respectively. We have used a zero-phase filter with these characteristics. We have added trace padding to avoid edge effects. In the padding region we have interpolated the traces using a trigonometric interpolation and with a Tukey window.

The processed shot-gather after step 3 is plotted in Figure 2b.

This processing improves SNR of records and allows detecting water layer reflections in shot-gathers, but there is still substantial noise related to ship-tow at the streamer frontal sections, and tail buoy jerking, random ocean noise, and weather-related swell noise present in the data. A common option to eliminate the tail buoy jerks and ocean noise is using frequency/wavenumber (FK) dip filtering; but FK filtering undesirably modifies the waveform of the direct wave. To avoid this we have done the following:

1. Separate the direct water wave from the reflected wavefield records. To do this we have first applied a linear move-out at acoustic speed in water. Then, we have normalized the maximum amplitudes, and applied a Singular Value Decomposition (SVD) [*Ferlin et al*., 2011]. We separate the shot-gather in two parts, the first one with the wavelet that correspond to the maximum eigenvalue of the SVD, SG_1, which mainly corresponds to the direct wave, and the second one with the rest of the record SG_2, that is to say, SG_2 is the original shot-gather after subtracting SG_1. We finally undo the linear move-out and the normalization in the two subrecords.
2. To reduce the swell noise, we first calculate a linear regression of the time shifts used in the previous step and then we eliminate the traces with time shifts that differs more than 0.01 s the linear regression. After that, we interpolate the eliminated traces using a *sinc* temporal interpolation with the Seismic Unix (SU) software [*Stockwell*, 1997] using the adjacent traces.
3. For SG_2, we apply a normal move-out and a dip-filter with amplitude 1 for the slopes inside the range $(1515 \pm 100\, m/s)^{-1}$ and zero outside to leave only the reflections caused by the source and the velocity water contrasts. Aliasing in the FK spectrum is avoided by interpolating traces. This step has been done using the SU software.
4. Finally, we sum the cleaned SG_1 and SG_2 subrecords to retrieve the complete shot-gather.

In Figure 2c, we show an example of the final, fully processed shot-gather. Tail buoy jerking has been effectively attenuated, but there is still some remaining swell noise and some noise from tow jerks in the frontal traces.

3.2. 2-D FWI of the Sound Speed

3.2.1. Misfit and Adjoint Method

In this section, we present the main points of the adjoint-state FWI strategy that we have followed, emphasizing the parts of the inversion scheme that we have specifically developed and implemented for water layer inversion, so that they differ from previous FWI studies in solid Earth research.

The adjoint-state FWI method originally proposed by *Lailly* [1983], and *Tarantola* [1984], is a data-fitting method used to extract physical parameters of the Earth using the seismic response of the medium that is contained in the recorded seismograms [*Virieux and Operto*, 2009]. The fitting is calculated by comparing the recorded data with synthetic data that are simulated numerically solving the wave equation in a reference model. Therefore, the difference between the reference model and the target model is reflected by differences in the seismic records. This difference is measured with an objective function, which in our case is the L2-norm,

$$\chi = \sum_{s,r} \int_{t=0}^{t_a} \mathbf{W}_1(\mathbf{r}_s, \mathbf{r}_r, t)\mathbf{W}_2(\mathbf{r}_s, \mathbf{r}_r, t)(u_s(\mathbf{r}_r, t) - c_{sr} d_s(\mathbf{r}_r, t - t_{sr}))^2 dt \quad (1)$$

where r and s are the labels for the receiver and the sources, $u_s(\mathbf{r}_r, t)$ is the synthetic wavefield, $d_s(\mathbf{r}_r, t)$ are the field data, $\mathbf{W}_1(\mathbf{r}_s, \mathbf{r}_r, t)$ represents a correction term, $\mathbf{W}_2(\mathbf{r}_s, \mathbf{r}_r, t)$ represents a weighting term, t_{sr} a time shift correction, c_{sr} is a calibration term, and t_a the acquisition time. t_a is fixed at $t_a = \frac{Z_{max}}{v_0}$ where $Z_{max} = 2$ km is the maximum depth of the target model and $v_0 = 1515$ m/s a mean water velocity.

The c_{sr} term is a calibration term to convert from pressure to the original data units, for example, Volts if a condenser is used to measure the pressure. We have calculated the calibration term independently for each pair source-hydrophone to use this term also as a correction term to reduce the source signature changes due to the irregular sea-surface conditions and the inhomogeneous source directivity. It is calculated by maximizing the overlap between the synthetic data and the real data [*Plessix et al*., 2012]. It reads as follows:

$$c_{sr}=\frac{\int_{t=t_0-1/f}^{t_0+1/f} u_s(\mathbf{r}_r,t)\,d_s(\mathbf{r}_r,t-t_{sr})}{\int_{t=t_0-1.5/f}^{t_0+1.5/f} d_s^2(\mathbf{r}_r,t-t_{sr})} \tag{2}$$

where $t_0=\frac{||\mathbf{r}_s-\mathbf{r}_r||}{v_0}$ is the travel time of the direct water wave in a velocity model of v_0 and f is the inverted frequency.

Data have phase misfits of a few milliseconds especially at large offsets due to the imperfect localization of the streamer hydrophones and also to the 2-D projection of the actual curved streamer geometry during the survey. To mitigate this we have added a time shift correction t_{sr} that corresponds to the maximum of the cross-correlation between the synthetic and field traces independently for each receiver,

$$t_{sr}=\arg\max_{\delta\in(t_0-1/f,t_0+1/f)}((u_s(\mathbf{r}_r)\star d_s(\mathbf{r}_r))(\delta)) \tag{3}$$

where $\star$ indicates the cross-correlation product.

The correction term $\mathbf{W}_1(\mathbf{r}_s,\mathbf{r}_r,t)$ has been introduced to remove spurious reflections. It eliminates the trace when its amplitude exceeds a physically plausible value. We fix this term to $R_{max}=0.015$, which corresponds to a jump of 23 m/s in a background of v_0, twice as larger as the strongest contrasts within the water layer based on local XBT data. This factor reads as

$$\mathbf{W}_1(\mathbf{r}_s,\mathbf{r}_r,t)=\begin{cases}1, & \text{if } d_s(x_r,t)<\dfrac{R_{\max}d_{\max}(x_s)}{G(\mathbf{r}_s,\mathbf{r}_r,t)}\sqrt{\dfrac{||\mathbf{r}_s-\mathbf{r}_{r1}||}{v_0t}}\\ 0, & \text{otherwise}\end{cases}. \tag{4}$$

where $G(\mathbf{r}_s,\mathbf{r}_r,t)=\frac{1}{1+\tan^2(\theta)}$ is the gain factor applied to compensate the amplitude dependence of the reflection coefficient with respect the incident angle $\theta=\arcsin\left(\frac{||x_s-x_r||}{v_0t}\right)$, and $d_{\max}(x_s)$ is the maximum amplitude of the source calculated measured at the nearest-offset receiver labeled with $\mathbf{r}_{r1}$.

For the second term $\mathbf{W}_2(\mathbf{r}_s,\mathbf{r}_r,t)$ we have included the gaining term $G(\mathbf{r}_s,\mathbf{r}_r,t)$ that is equal to the simplification of the Zoeppritz equation proposed by *Shuey* [1985] to increase the weight of small amplitude reflections in the misfit function. Moreover, we have compensated the 2-D amplitude decay multiplying by $\sqrt{t}$ and we have equalized the energy of the shots dividing by the total source energy $E_s=\int_{t=0}^{t_a}s_s(t)^2dt$:

$$\mathbf{W}_2(\mathbf{r}_s,\mathbf{r}_r,t)=\frac{\sqrt{t}\,G(\mathbf{r}_s,\mathbf{r}_r,t)}{E_s} \tag{5}$$

To calculate the misfit function we have simulated the pressure wavefield propagation by solving the following differential equation:

$$\frac{1}{\kappa(\mathbf{r})}\ddot{u}_s(\mathbf{r},t)+\nabla\cdot\left(\frac{1}{\rho(\mathbf{r})}\nabla u_s(\mathbf{r},t)\right)=s_s(\mathbf{r},t) \tag{6}$$

where $\kappa(\mathbf{r})$ and $\rho(\mathbf{r})$ are the compressibility and the density of the medium, respectively. We have implemented a numeric algorithm to integrate the wave equation with a finite difference scheme. For this we use a Runge-Kutta method of fourth order in time [*Lambert*, 1991]. The space discretization is done using a staggered grid between the pressure field and the pressure flux with a sixth order Taylor expansion. To absorb the spurious reflections in the left, right and bottom boundaries of the model that would dominate over the real ones, we have implemented a complex-frequency-shifted perfectly matched layer (CFS-PML) [*Zhang and Shen*, 2010] with 15 layers and the parameters listed in the supporting information. For the top boundary we make use of two ghost layers above the model surface where the pressure field is fixed using an image criterion as suggested by *Zhang and Chen* [2006], and in the surface the pressure is fixed to zero.

This warrants the reflection of the incident waves with a π phase shift as it happens in the water-air interface. The values of the velocity field in the ghost layers is fixed so that the waves propagate according with equation (6).

The source signature in equation (6) is inverted by minimizing the misfit function in terms of the source signature in frequency domain, as proposed by *Pratt* [1999]. This leads to the following equation:

$$s_s(\omega) = \frac{\sum_r d_s^*(\mathbf{r}_r, \omega) u_s(\mathbf{r}_r, \omega)}{\sum_r u_s^*(\mathbf{r}_r, \omega) u_s(\mathbf{r}_r, \omega)} s_{s,0}(\omega) \tag{7}$$

where $s_s(\omega)$ is the source signature that corresponds to the shot located in the position $\mathbf{r}_s$, ω indicates the functions are expressed in frequency domain, and $u_s(\mathbf{r}, \omega)$ is the synthetic wavefield calculated using the source signature of the previous iteration $s_{s,0}(\omega)$. For the first iteration we assume a Ricker function with a frequency centred at the inversion frequency. The inverted source is then used as input in the subsequent inversion steps. This is repeated for all the individual shots.

Once we have calculated the misfit and the source wavelet, the reference model is perturbed in order to reduce the misfit in a search direction that follows the gradient of the misfit versus the model parameter to be inverted. Due to the huge computational cost that a direct calculation of the derivatives involved in the gradient would have, we use instead the adjoint method proposed by *Lailly* [1983], and *Tarantola* [1984]. In the adjoint formulation, the gradient corresponds to the correlation between the forward wavefield and the back-propagated residual wavefield, or adjoint field, as follows

$$\mathrm{g}_\kappa(\mathbf{r}) = \sum_s \frac{1}{\kappa(\mathbf{r})} \int_{t=0}^{t_a} \dot{u}_s(\mathbf{r})\, \dot{u}_s^\dagger(\mathbf{r}) \tag{8}$$

where $u_s^\dagger(\mathbf{r})$ is the adjoint wavefield, which is calculated resolving the wave equation with the adjoint source

$$s_s^\dagger(\mathbf{r}, t) = -\sum_r \mathbf{W}_1(\mathbf{r}_s, \mathbf{r}_r, t) \mathbf{W}_2(\mathbf{r}_s, \mathbf{r}_r, t)\, (u_s(\mathbf{r}_r, t) - c_{sr}\, d_s(\mathbf{r}_r, t - t_{sr})) \delta(\mathbf{r} - \mathbf{r}_r) \tag{9}$$

and g_κ is the gradient of the misfit with respect to $\kappa(\mathbf{r})$. In the following we only invert sound speed because this property is the main contributor to water reflectivity [*Sallarès et al.*, 2009].

To calculate the product of the adjoint field and the forward field of equation (8), we first propagate the forward field to calculate the adjoint source and at the same time we save the value of the field at the boundaries of the model (before the CFS-PML) as well as the whole field at the last iteration. Second, we propagate the adjoint field and back-propagate the forward field using the field at the last iteration and the values of the field at the boundaries to recover the wavefield that exists the model (without the source term and CFS-PMLs). Using this methodology we avoid saving the whole forward wavefield to calculate the gradient, reducing in more than one order of magnitude the memory requirements.

3.2.2. Gradient Preconditioning and Search Direction

The objective of the inversion is to account for the difference in the shot-gathers caused by sound speed differences within the reference model. Considering only one shot-gather, the reflector positions that are reflected in the gradient maps are accurate just below the streamer location, while significant artefacts appear outside of this region. These artefacts are a consequence of the divergence effect that appears when a delta source is considered in a finite difference solver, the notch reflection that, combined with the imperfect source inversion, can cause interference delays, the presence of low wavenumber errors in the reference model and remaining noise in the shot-gather.

To adapt the point source to the grid instead of a delta function we consider a band-limited delta function including frequency content below the Nyquist frequency. To limit the spatial spreading of the resulting *sinc* function we also apply a Hann window with a maximal size of 8 points of the grid.

High-wavenumber components tend to appear in the gradient as a consequence of the noise in the data and the sensitivity of the gradient to the acquisition geometry [*Mora*, 1989]. For the gradient of an individual shot, these errors are clearly visible away of the streamer. Thus, we have applied a weighting term, which

is equal to one below the range between the source point and the end of the streamer, and it decays exponentially to zero in the horizontal direction outside this range:

$$\mathbf{O}_{x_s}(x,z)=\begin{cases}1 & \text{if } x\in[x_s,x_{s,rl}]\\ \exp\left(-\left(\frac{x-x_s}{\sigma_d}\right)^2\right) & \text{if } x<x_s\\ \exp\left(-\left(\frac{x-x_{s,rl}}{\sigma_d}\right)^2\right) & \text{if } x>x_{s,rl}\end{cases}. \tag{10}$$

Here, $\sigma_d = 50$ m and $x_{s,rl}$ is the last receiver of the streamer when the source is located at x_s. This weighting term has been applied for each individual gradient before summing the contributions of the different shot to generate the complete gradient.

Additionally, we also introduce another weighting term to increase the weight of the gradient in the central depth of the model at 1.5 km:

$$\mathbf{P}(x,z)=\left(1+a\frac{z}{Z_{\max}}\right)\left(1-a\frac{z-Z_{\max}}{Z_{\max}}\right) \tag{11}$$

where a is fixed to 3.

The parametrization of the model has a drastic effect in the convergence of the minimization algorithm as shown by *Köhn et al*. [2012], and *Guitton et al*. [2012]. For such a reason, instead of using the compressibility, $\kappa(\mathbf{r})$, as parametrization of the model, we choose a power of $\kappa(\mathbf{r})$ of 0.75 as model parametrization because it shows a better performance reducing the number of iterations as shown by *Dagnino et al*. [2014].

After calculating the gradient in the new parametrization we apply a smoothing regularization operator, $\mathbf{F}_{\lambda_x,\lambda_z}$, to remove possible artefacts. This operator is implemented using a 2-D low-pass zero-phase Butterworth filter with a padding term in the border of the model to avoid edge effects. The high-cut spatial frequencies of the model are adapted to the inverted frequency as suggested by *Ravaut et al*. [2004], choosing an average wavelength of $\lambda_x = p_x\, v_0/f$ and $\lambda_z = p_z\, v_0/f$ for the horizontal and vertical component, respectively. The weights p_x and p_z used to define the low wavelength cut of the filter are fixed to 0.3 and 0.1, respectively.

Low frequency artefacts in the gradient produced by the 2-D approximation cause the gradient to contain wavenumbers that are smaller than those being actually inverted. To mitigate these artefacts we have applied a high-pass filter in the gradient with a cutting wavelength of 2.5 v_0/f in the vertical direction.

Finally, we obtain as a preconditioned search direction:

$$\Lambda=-\mathbf{F}_{\lambda_x,\lambda_z}\left[\mathbf{P}\sum_{s=1}^{n_s}\mathbf{O}_{x_s}\,g_{k^m}\right] \tag{12}$$

, for simplicity, the coordinate dependence (x, z) is not specified.

After several tests with more sophisticated choices, and in particular the quasi-Newton limited-memory Broyden-Fletcher-Goldfarb-Shanno (l-BFGS) algorithm [*Nocedal*, 1980], we have decided to use the simplest search direction method: the steepest descent. The reason for this is that, even if l-BFGS greatly accelerates convergence, it is also highly sensitive to noise because it enhances the effect of small reflections. In general, this is positive for the inversion but, in our case, most of the small amplitude signal is due to remaining noise, and the tests made show that its effect is too large and inversion does not converge.

Once the gradient has been calculated and preconditioned, the step length $\alpha^{(k)}$ (k indicates the iteration number) is determined perturbing the velocity model, calculating the misfit and interpolating to find the minimum on the search direction, i.e., $\alpha^{(k)}=\arg\min_{\epsilon}\left(\chi\left(m^{(k)}-\epsilon\,\Lambda^{(k)}\right)\right)$ where the first step tested is $\alpha^{(k)}=\alpha^{(k-1)}\frac{\Lambda_{k-1}^T\Lambda_{k-1}}{\Lambda_k^T\Lambda_k}$.

The stopping criteria that we use in the inversion is the Arminjo rule [*Nocedal and Stephen*, 2006].

3.2.3. Initial Model Building

When the reference model is too far from the true solution, it might happen that the starting model does not contain the correct kinematic information [*Virieux and Operto*, 2009; *Mulder and Plessix*, 2008]. In this case, the synthetic and recorded seismogram will differ in more than a half a period for a given initial inversion frequency, causing that the minimization algorithm ends in a local minimum.

Different options have been proposed to overcome this limitation, for instance changing the objective function for a more robust one [*Jiménez Tejero et al*., 2015], or applying of a time window to select only early arrivals (refractions) that are chiefly affected by the background properties of the model [*Brenders and Pratt*, 2007]. Given the low SNR and the absence of refractions due to the weak vertical V gradient in the water layer, these techniques are not adequate to our case. Alternative strategies have been explored to overcome the above-mentioned limitations and generate suitable reference models. These include the use of global, instead of local, inversion methods such as genetic algorithms [*Padhi et al*., 2015], or the application of Laplace and Laplace-Fourier domain, rather than time domain, inversion [*Blacic et al*., 2016]. As stated in the introduction, the first approach has been shown to work under certain circumstances, but the computational burden is very large. The second approach has only been tested with synthetic data, under the assumption of a data set containing unlimited low frequencies (0–2.5 Hz), which is not the case.

The goal of our work is to demonstrate that adjoint-state FWI can be used to obtain high-horizontal resolution models of the water properties when we have a suitable reference model; this is, a model that allows overcoming cycle-skipping at the lowest available frequency of the data set. This step is critical in our case, because the lowest usable frequencies in the data set to be inverted are ∼10 Hz, at least one octave higher than those commonly present in solid Earth recordings (3–5 Hz). As in previous works [e.g., *Papenberg et al*., 2010; *Biescas et al*., 2014], we take advantage of the availability of complementary oceanographic data, and in particular in situ measures of water properties such as T, S or V along vertical soundings using probes. XBTs and conductivity-temperature-depth probes (XCTDs) are particularly useful for our purposes because they can be deployed at low cost from the seismic vessel simultaneously to the seismic acquisition.

During the GO survey, XBTs were deployed every ∼2.5 km coeval to seismic acquisition, a distance that determines the horizontal resolution of the probe-based V, T and/or S models. These are the data that we have used for building the reference model to start FWI (Figure 3a). To minimize numerical dispersion of the finite difference solver we have linearly interpolated the 1-D V profiles obtained with the individual XBTs at 5 m both horizontally and vertically, and we have then filtered them at 200 m to remove artefacts that appear as spurious reflectors due to the horizontal interpolation. The resulting XBT-based reference model, used as initial model to start the inversion, is shown in Figure 3a.

3.2.4. Multiscale Inversion Strategy

A common procedure to help mitigating the effects of nonlinearity is to use a multiscale strategy, which consists of inverting hierarchically different frequency bands from the lowest to the highest ones [*Bunks*, 1995]. The data-frequency content in each step of the multiscale strategy is limited by applying a low-pass Butterworth filter to the processed seismic traces. The tests made indicate that water reflectivity at frequencies higher than 20–25 Hz is too faint to provide additional details to the V model. Therefore, we decided to perform two inversion steps with high-cut frequencies of 15 Hz and 25 Hz. The probe-based V reference model (Figure 3a) is used as initial model in the first step, and the resulting model after the first step is used as initial model in the second step.

To perform the inversion we have used the acoustic version of the ElasInv2-D code [*Dagnino et al*., 2014] with several modifications. The algorithm is parallelized with message passing interface standards. This parallelization distributes the wavefield propagation of all the shots among the available computational resources. For this work, we have used 4 cluster nodes with two Quad-Core Intel(R) Xeon(R) E5640 2.67 GHz Processors. The model has been divided in 9 parts of 6–7 km containing 120–140 shots each; and the simulation of the forward and adjoint wavefields have been distributed over 32 cores. The computational time to finish the inversion for each part of the model is ∼30 h, so 270 h in total. In other words, 4.5 h per km with 32 cores.

The final V model is shown in Figure 3b. Convergence is achieved after ∼25 iterations. This improvement becomes evident if we compare the seismograms simulated with the reference and final V models (Figures 4a and 4b, respectively) with those actually recorded in the streamer channels (Figure 4c). A number of reflections that are not present in the reference model data do appear when we use the final one.

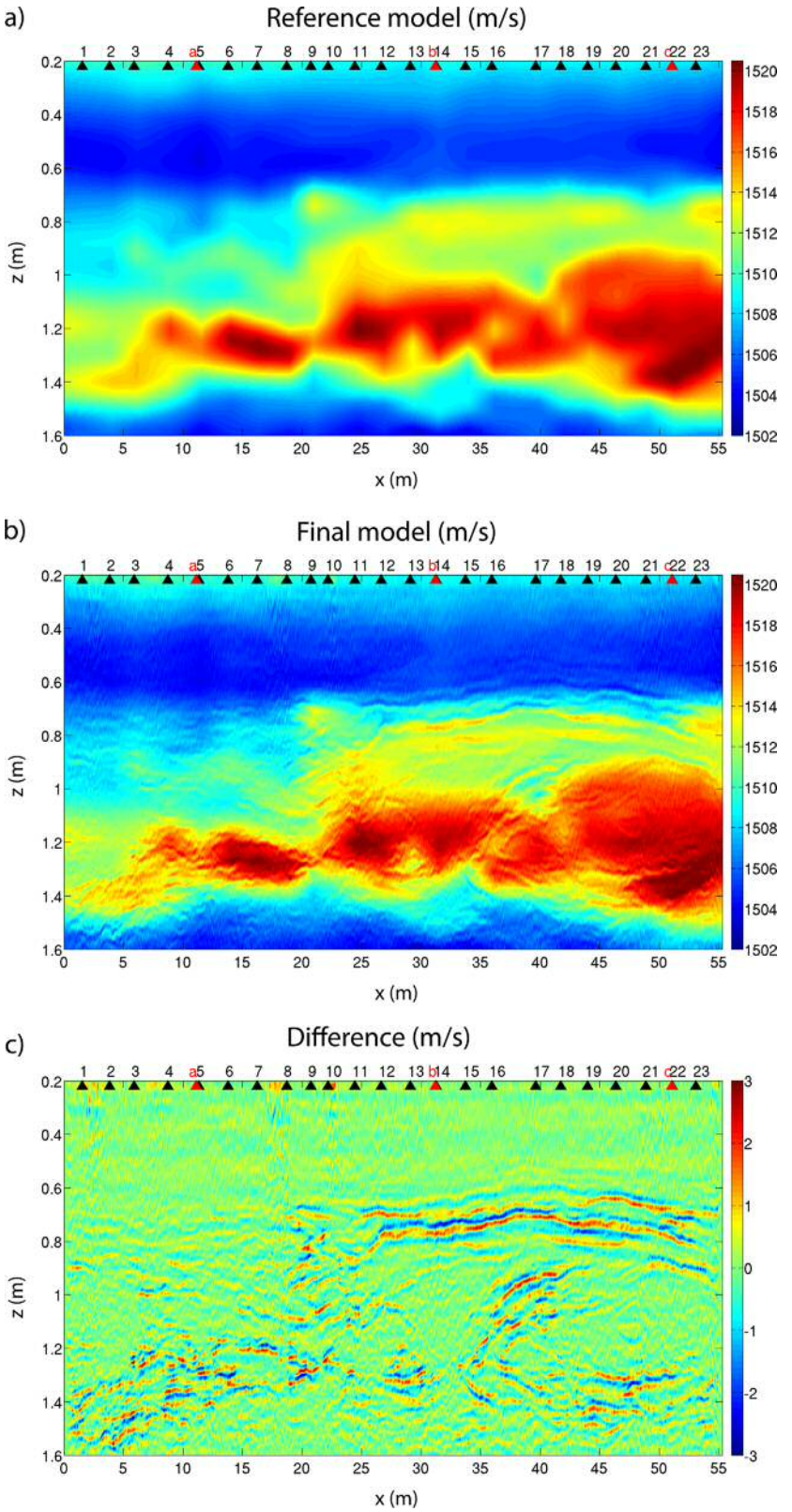

Figure 3. (a) Reference velocity model build interpolating and filtering the XBT data. (b) Final velocity model obtained after FWI inversion of the MCS data. (c) Difference between the reference and final sound speed model. The position all the XBTs are represented by black numbered triangles in the top of the model. The position of the CTDs deployed are represented with red triangles and labeled with Roman letters.

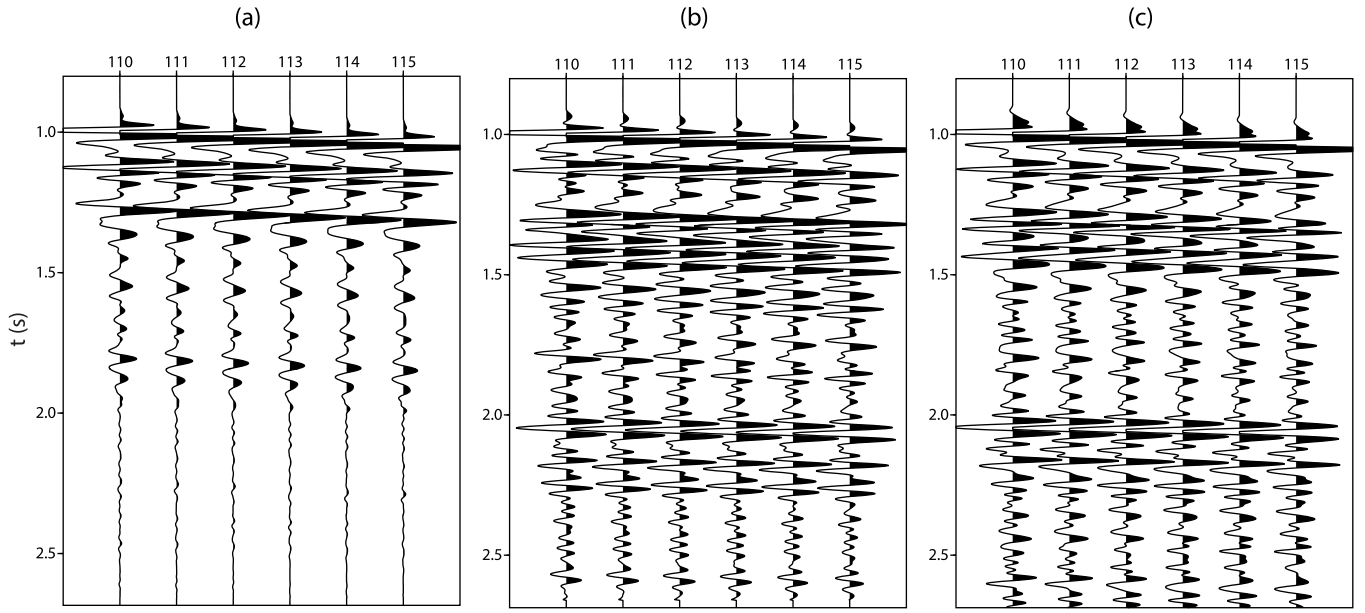

Figure 4. To compare the data-fitting obtain with FWI, we plot the traces from 110 to 115 of one shot located at 6656 m of the initial point of the seismic line. Vertical axis indicates two-way time in seconds. (a and b) The synthetic traces calculated using the initial and the final model, respectively. (c) The real pressure field measured by the hydrophones at the same traces.

3.2.5. Temperature and Salinity Retrieval From Sound Speed

In this work we have inverted a single parameter (V), following a strategy that is similar to that of previous inversion works [*Papenberg et al.*, 2010; *Biescas et al.*, 2014]. In this approach, T and S are obtained from V using two equations that relate the three parameters. One equation is the thermodynamic equation of seawater [*Fofonoff and Millard*, 1983], which allows expressing V as a function of T, S and pressure (P), but a second one is needed to separate the effects of T and S. Therefore, we use a P-dependent T-S relation inferred from regional data of the National Oceanic and Atmospheric Administration (NOAA) database [*Boyer et al.*, 2013]. This relationship displays an approximate linear dependence between T and S for a given P as shown in the supporting information. We first calculate V from T and depth using the thermodynamic equation of seawater, introducing S as a function of T using the T-S relation. Then we minimize the difference between this V value and the inverted one. Once we get T that minimizes the difference, S is obtained applying the T-S relation.

The main steps of the method applied are the following ones:

1. We selected all high resolution CTD data between 37.5° and 35.0° and −10° and −6° collected after 1990 reaching our maximum target depth of 1.8 km from the NOAA database. We eliminated profiles displaying T jumps larger than 2°C in less than 5 m, since they are suspicious to have spurious values after individual quality control of some files. The resulting data set after this step is composed of 118 CTDs.
2. To calculate the functional relation between T and S, we have assumed a linear dependency at each depth, i.e., $T(S,z)=A(z)+B(z)S(z)$ where $A(z)$ and $B(z)$ are the fitting coefficients and $S(z)$ is salinity at each depth z. We performed a linear least square fitting to obtain the coefficients $A(z)$ and $B(z)$.
3. We applied the thermodynamic equation of seawater that relates V, T, S and P (from latitude and depth) using the "Gibbs-SeaWater Oceanographic Toolbox" from the TEOS-10 software [*McDougall and Barker*, 2011].
4. At this stage, we have V as a function of S and T; i.e., $V^{TEOS}(S,z)=V_{GSW}(T(S),S,z)$, where V_{GSW} is the thermodynamic equation of seawater, $T(S)$ the T-S relation and z the depth. Finally, we minimized the absolute difference between $V^{TEOS}(S,z)$ and the sound speed obtained from the FWI using the Newton's method to obtain S and T from the T-S relation. The resulting T and S models are shown in Figures 5 and 6.

In order to compare the influence of the data set used to calculate the T-S relation, we have also used the previous work-flow using 41 CTD profiles collected by a second vessel during the survey (the German R/V Poseidon). These data are not simultaneous to the MCS acquisition; the time difference was of ∼3 h in average. Three of the CTD were not used to estimate the T-S relationships, but used as a reference to compare with the inverted models.

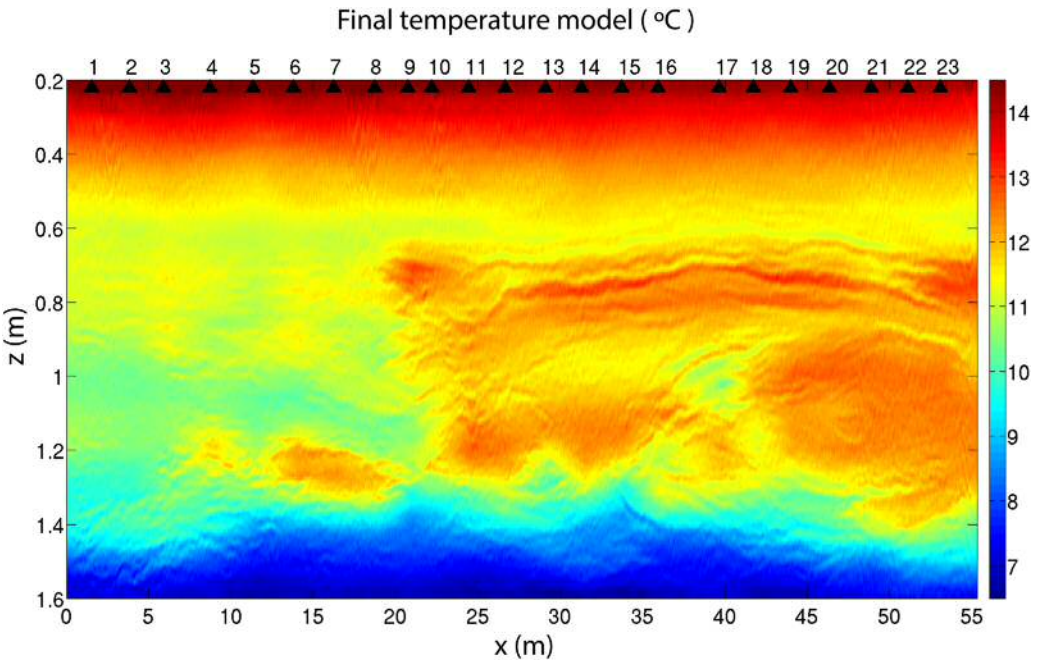

Figure 5. Final temperature model obtained from the sound speed using the thermodynamic equation of seawater and the NOAA data set. The position of the XBTs deployed are represented with black triangles. In the supporting information, we show the comparison between the final T model and the T XBT vertical profiles to show how SO can help to correlate structures.

4. Results and Discussion

The reference and inverted V models are shown in Figures 3a and 3b, respectively, and the difference between these two is shown in Figure 3c. These differences reflect information on the water layer properties that is not present in the smoothed probe-based oceanographic data but in the MCS data.

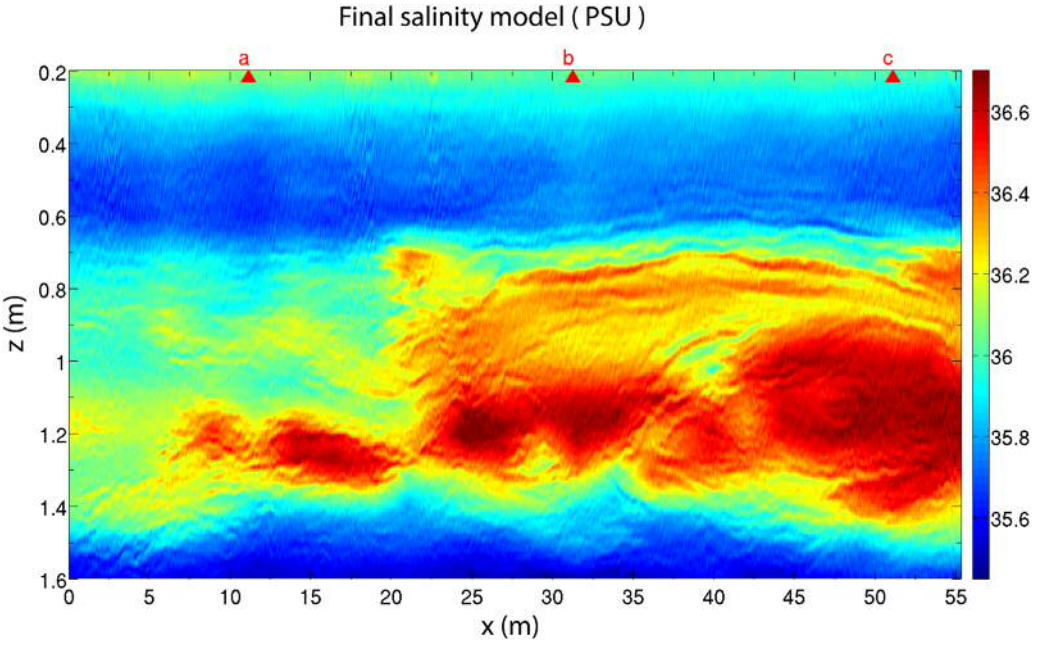

Figure 6. Final salinity model obtained from the sound speed using the thermodynamic equation of seawater and the NOAA data set. The position of the CTDs deployed are represented with red triangles.

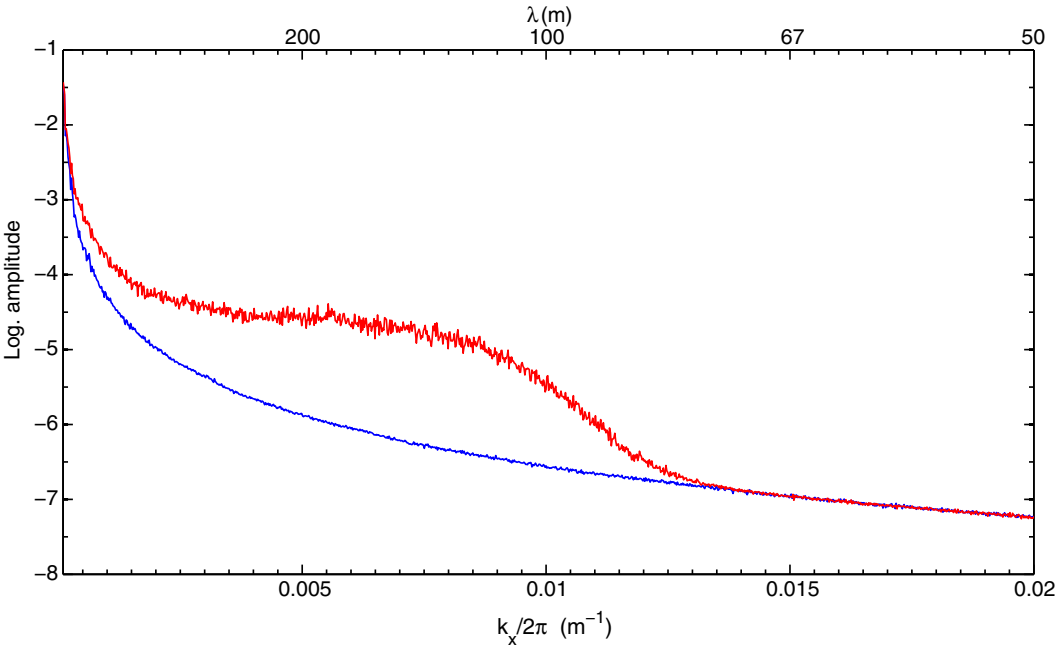

Figure 7. Logarithm of the mean amplitude component of the Fourier decomposition in the horizontal axis. The blue line corresponds to the initial velocity model and the red line the final velocity model. Vertical axis is dimensionless because the logarithm is calculated after dimensional normalization of the amplitudes. Horizontal axis contains (top) the wavelength of the Fourier mode and (bottom) the wavenumber divided by 2π.

The theoretical lateral resolution of the models obtained by FWI is $R_x \approx \lambda$, where λ is the maximum inverted wavelength; so that $R_x \approx$ 60–75 m in our case, because the maximum inverted frequency is 20–25 Hz. To confirm this, we have compared the logarithm of the mean amplitude of the Fourier decomposition components in the horizontal axis for the reference and inverted V models summing for all depths (Figure 7). In this figure the vertical axis is dimensionless because the logarithm is calculated after dimensional normalization of the amplitudes, whereas the horizontal axis represents the horizontal wavenumber/wavelength of the corresponding Fourier mode. The amplitude of the Fourier components is larger in the inverted than in the reference model for wavelengths between ∼70 m and ∼2000 m, reflecting the range of horizontal scales at which information that is not contained in the smooth probe-based models can be extracted from the MCS data.

In both, XBT-derived and MCS-inverted models it is possible to identify the Mediterranean Water (MW) mass occupying the layer between 700 m and 1500 m deep, surrounded on top by the Atlantic Intermediate Water and below by the North Atlantic Deep Water. Hence, the information of the mesoscale current is detected by both data sets. However, MCS-inverted model significantly improves the detection of submesoscale and fine structures, which are in the lateral wavelength range between ∼70 m and ∼2000 m. There are distinct regionally continuous oceanographic features that cannot be identified without the help of the MCS data. In particular, laterally continuous thermohaline layers, which appear at the top of the MU, and thermohaline intrusions that can be seen at the horizontal fronts, for example at 5 km, 20 km and 40 km distance along the profile (Figures 5 and 6). Besides, T and S inverted models show that there is a warmer and saltier structure inside the MW layer that could be interpreted as a section of a Meddy based on the concave shape and layered top of the structure, the spiral-arms-like features developed between 5 km to 20 km [*Song et al*., 2011] and on the fact that this area is prone to Meddy generation.

It must be noted that conventional, probe-based oceanographic measures have an observational gap at horizontal scales of 10^3 m to 10^1 m [e.g., *Müller et al*., 2005]. The availability of an observational system providing information on the variability of physical parameters within this range of scales should help to understand the physical processes that control the transition from anisotropic internal wave motions to isotropic turbulence, which at present are only partially observed in the ocean and poorly understood [e.g., *Ferrari and Wunsch*, 2009; *Sallarès et al*., 2016].

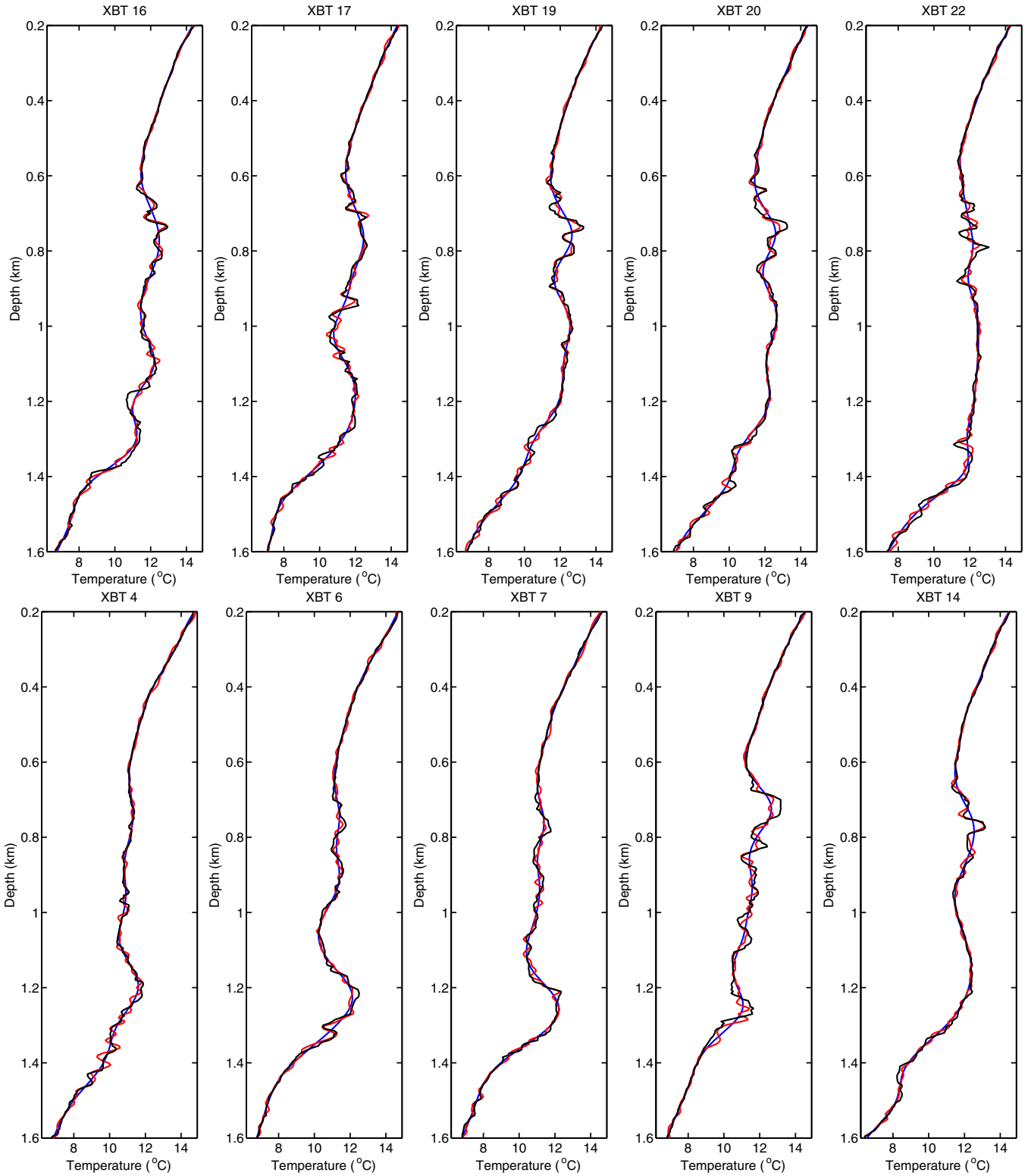

Figure 8. Comparison between 1-D temperature-depth profiles taken from the initial (blue line) and final (red line) models of the FWI, and those measured with the XBTs (black line). This is plotted for 10 XBTs corresponding to the positions labeled with 4, 6, 7, 9, 14, 16, 17, 19, 20, 22 in Figures 3a and 3b.

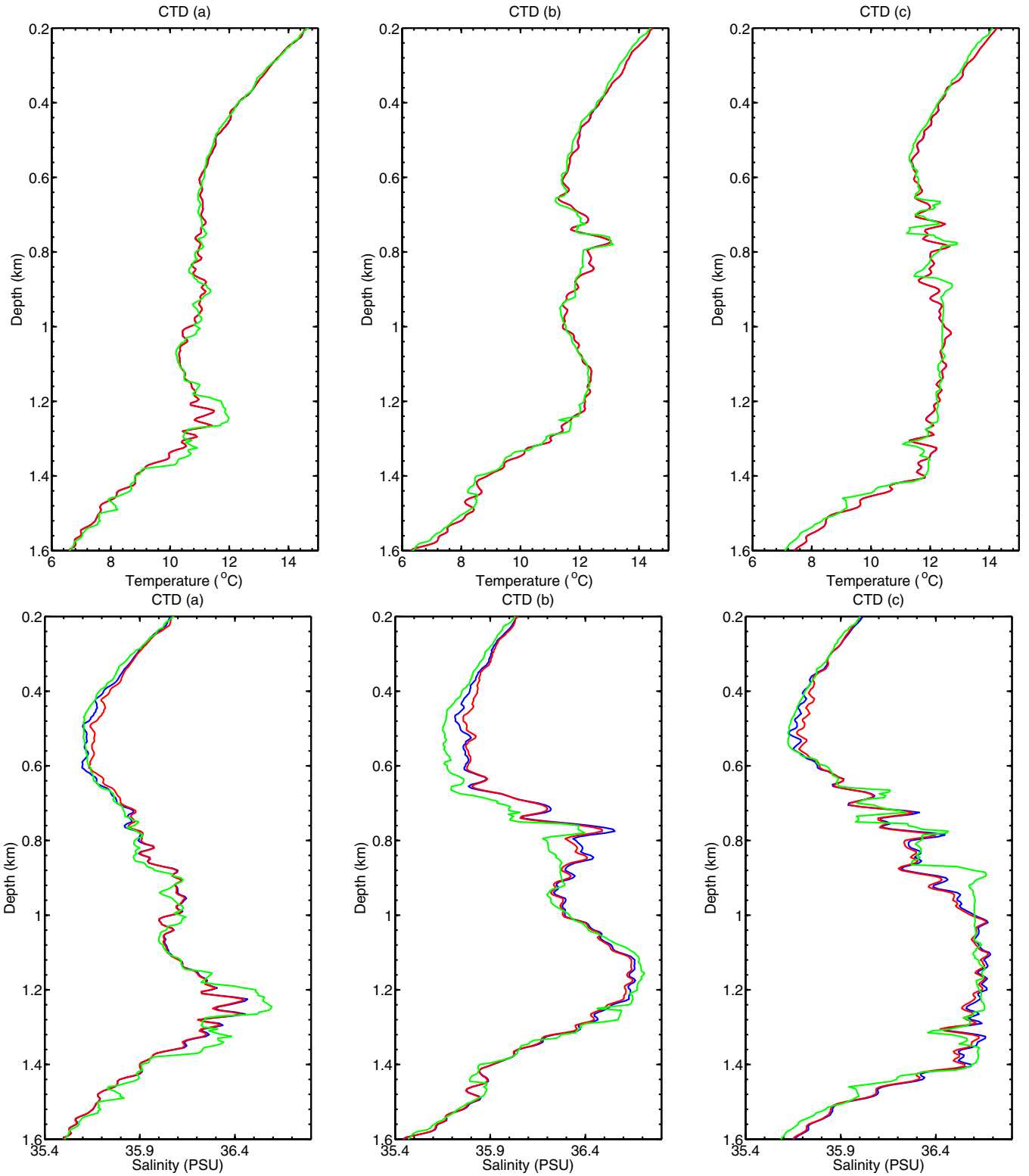

Figure 9. (top) Comparison between the CTD temperature profiles collected by R/V Poseidon ∼ 2–3 h after the MCS acquisition (green line), and 1-D temperature-depth profiles extracted from the T model shown in Figure 5 (red line), and the final temperature model calculated using the T-S relation from the CTDs collected by Poseidon instead of the NOAA compilation (blue line). Both T profiles obtained from Figure 5 and the analogue profile calculated using the CTDs collected by Poseidon give similar T results, so it is difficult to see the blue lines that is overlapped by the red one. We plot the three CTD corresponding to the positions (a), (b) and (c) shown in Figure 5. (bottom) Comparison between the CTD salinity profiles collected by the Poseidon boat ∼2–3 h after the shots (green line), the final temperature model calculated using the T-S relation from NOAA data set (red line), and the final temperature model calculated using the T-S relation from the CTD collected by Poseidon (blue line). We plot the three CTD corresponding to the positions (a), (b) and (c) shown in Figure 6.

4.1. Accuracy of the Inverted T and S Models

One advantage of water layer vs solid Earth inversion is that in the first it is possible to directly estimate the accuracy of the obtained models (i.e., the errors of the inverted parameters) by computing the difference between the inverted parameters and the ones measured by simultaneous relatively closely spaced oceanographic probing along the profile. In our case, we have measured the difference between 1-D vertical profiles from the inverted T model at the XBT locations and the actual T values measured by the XBTs. In Figure 8 we show the comparison between the XBT measures and the final inverted T model. The standard deviation of T between both the two vertical profiles for all the XBTs that fall inside the model is of 0.18°C. The difference between XBT and our results is understood as a quality control and a measure of the error. The result is very similar if we use for the comparison one XBT that has not been used to construct the reference model (Figure 3a). Unfortunately, XBTs do not have S information. During the GO experiment, a number of XCTDs, which do provide S measurements, where deployed along some MCS lines, but not along our segment of the LR10. In this case, the estimation of the accuracy is done comparing with the CTD measures done by the German R/V Poseidon on average 2–3 h after the seismic acquisition which gives a standard deviation of 0.08 PSU. Therefore, in this case the difference between inverted and measured S (and T) does not only reflect inversion inaccuracies but also the effect of actual movement of the imaged structures of the water layer. The results of the comparison for the three CTDs deployed along the LR10 line are shown in Figure 9. For T, the average deviation between the inverted models and the CTD measures are of 0.24°C, 1.3 times larger than the difference between the model and the XBT measures, reflecting the influence of moving water masses.

5. Conclusions

This works demonstrates the feasibility of 2-D adjoint-state acoustic FWI of prestack marine MCS data to retrieve V, T, S models with high horizontal resolution. For this we propose a strategy that combines (1) a specifically designed MCS data processing flow that aims at reducing acoustic noise without affecting the direct wave, and (2) a multiscale FWI scheme that includes sound speed and source wavelet inversion with gradient preconditioning and inversion regularization constraints that are also specific for water layer inversion. The complete data processing and inversion sequence proposed is semi-automatic, so it can be adapted to other data set with minor modifications and moderate testing.

The novel aspects of the data preconditioning flow are the shot gather processing to separate the direct wave contribution from the water reflections, and the application of frequency- and dip-filters that exploits the velocity constraints in the water layer to increase the SNR while preserving the waveforms, which is necessary for a successful FWI. In the inversion steps, the new elements include a quality control that uses a physical constraint based on the maximum reflection that is plausible in the water layer; and the inclusion of energy equalization and gaining terms in the misfit function to equalize the amplitudes of the different reflection events. Other specific regularization terms are limiting the gradient contributions just below the streamer to increase weighting in the central part of the model, and a smoothing operator to eliminate artefacts with wavenumbers that do not correspond to the source frequency.

We demonstrate the efficiency of the proposed method by retrieving a 2-D sound speed model along a 55 km-long MCS profile collected in the Gulf of Cadiz during the GO experiment. We have also obtained 2-D T and S maps by combining the inverted sound speed model with the thermodynamic equation of seawater and a local, depth-dependent T-S relation derived from regional CTD data. The comparison of the inverted T, S models with simultaneous measures from XBT probes and also CTD probes deployed with a time delay of ∼2–3 h, show that the accuracy of the inverted models is 0.18°C for temperature and 0.08 *PSU* for salinity. A spectral analysis indicates that the horizontal resolution of the inverted V, T and S models ∼70 m. These results demonstrate the potential of MCS data to cover the observational gap that exists in oceanographic measurements at horizontal scales of 10^3 – 10^1 m. Obtaining information on the structures and processes occurring at these scales will contribute to better understand the mechanisms driving the energy transfer between the internal wave and turbulent subranges and how does it influence to mixing.

Acknowledgments
This is a partial contribution of the Barcelona Center for Subsurface Imaging. The work has been partially supported by the projects KALEIDOSCOPE and CO-Dos financed by REPSOL and MINECO project POSEIDON (CTM2010-21569) and HADES (CTM2011-30400-C02). B. Biescas work has been funded by the European Commission through the Marie Curie Action FP7-PEOPLE-2012-COFUND-600407. We acknowledge the EU-funded GO-project EC-NEST-15603 and the RRS Discovery (cruise D318) for the experimental data set that are available at https://www.bodc.ac.uk/data/information_and_inventories/cruise_inventory/report/8182/under request to the PI. We thank R. Hobbs and an anonymous reviewer for their suggestions for improving the quality of the manuscript.

References

Ambar, I., N. Serra, M. J. Brogueira, G. Cabeçadas, F. Abrantes, P. Freitas, C. Gonçalves, and N. Gonzalez (2002), Physical, chemical and sedimentological aspects of the Mediterranean outflow off Iberia, *Deep Sea Res., Part II*, *49*(19), 4163–4177, doi:10.1016/S0967-0645(02)00148-0.

Armi, L., D. Hebert, N. Oakey, J. F. Price, P. L. Richardson, H. T. Rossby, and B. Ruddick (1989), Two years in the life of a Mediterranean Salt Lens, *J. Phys. Oceanogr.*, *19*(3), 354–370, doi:10.1016/S0967-0645(02)00148-0.

Biescas, B., V. Sallarès, J. L. Pelegrí, F. Machín, R. Carbonell, G. Buffett, J. J. Dañobeitia, and A. Calahorrano (2008), Imaging meddy finestructure using multichannel seismic reflection data, *Geophys. Res. Lett.*, *35*, L11609, doi:10.1029/2008GL033971.

Biescas, B., L. Armi, V. Sallarès, and E. Gràcia (2010), Seismic imaging of staircase layers below the Mediterranean Undercurrent, *Deep Sea Res., Part I*, *57*(10), 1345–1353, doi:10.1016/j.dsr.2010.07.001.

Biescas, B., B. R. Ruddick, M. R. Nedimović, V. Sallarès, G. Bornstein, and J. F. Mojica (2014), Recovery of temperature, salinity, and potential density from ocean reflectivity, *J. Geophys. Res. Oceans*, *119*, 3171–3184, doi:10.1002/2013JC009662.

Blacic, T. M., H. Jun, H. Rosado, and C. Shin (2016), Smooth 2-D ocean sound speed from Laplace and Laplace-Fourier domain inversion of seismic oceanography data, *Geophys. Res. Lett.*, *43*, 1211–1218, doi:10.1002/2015GL067421.

Bornstein, G., B. Biescas, V. Sallarès, and J. F. Mojica (2013), Direct temperature and salinity acoustic full waveform inversion, *Geophys. Res. Lett.*, *40*, 4344–4348, doi:10.1002/grl.50844.

Bower, A. S. (2002), Structure of the Mediterranean Undercurrent and Mediterranean Water spreading around the southwestern Iberian Peninsula, *J. Geophys. Res.*, *107*(C10), 3161, doi:10.1029/2001JC001007.

Boyer, T. P., et al. (2013), *World Ocean Database 2013*, edited by S. Levitus, and A. Mishonov, 209 pp., NOAA Atlas NESDIS, 72, Silver Spring, Md.

Brenders, A. J., and R. G. Pratt (2007), Full waveform tomography for lithospheric imaging: Results from a blind test in a realistic crustal model, *Geophys. J. Int.*, *168*(1), 133–151, doi:10.1111/j.1365-246X.2006.03156.x.

Buffett, G. G., B. Biescas, J. L. Pelegrí, F. Machín, V. Sallarès, R. Carbonell, D. Klaeschen, and R. Hobbs (2009), Seismic reflection along the path of the Mediterranean Undercurrent, *Cont. Shelf Res.*, *29*(15), 1848–1860, doi:10.1016/j.csr.2009.05.017.

Bunks, C. (1995), Multiscale seismic waveform inversion, *Geophysics*, *60*(5), 1457, doi:10.1190/1. 1443880.

Dagnino, D., V. Sallarès, and C. R. Ranero (2014), Scale- and parameter-adaptive model-based gradient pre-conditioner for elastic full-waveform inversion, *Geophys. J. Int.*, *198*(2), 1130–1142, doi:10.1093/gji/ggu175.

Dietrich, M., and F. Kormendi (1990), Perturbation of the plane-wave reflectivity of a depth-dependent elastic medium by weak inhomogeneities, *Geophys. J. Int.*, *100*(2), 203–214, doi:10.1111/j.1365-246X.1990.tb02480.x.

Eakin, D., W. S. Holbrook, and I. Fer (2011), Seismic reflection imaging of large-amplitude lee waves in the Caribbean Sea, *Geophys. Res. Lett.*, *38*, L21601, doi:10.1029/2011GL049157.

Ferlin, A., L. Perilli, L. Gianesello, G. Taglialavoro, and C. Foresta (2011), Profiling Insulin Like Factor 3 (INSL3) signaling in human osteoblasts, *PLoS ONE*, *6*(12), e29,733, doi:10.1371/journal.pone.0029733.

Ferrari, R., and K. L. Polzin (2005), Finescale structure of the T S relation in the eastern North Atlantic, *J. Phys. Oceanogr.*, *35*(8), 1437–1454, doi:10.1175/JPO2763.1.

Ferrari, R., and C. Wunsch (2009), Ocean circulation kinetic energy: Reservoirs, sources, and sinks, *Annu. Rev. Fluid Mech.*, *41*(1), 253–282, doi:10.1146/annurev.fluid.40.111406. 102139.

Fofonoff, N. P., and R. C. Millard (1983), Algorithms for computation of fundamental properties of seawater, *UNESCO Tech. Pap. Mar. Sci.*, 44, UNESCO, Paris.

Guitton, A., G. Ayeni, and E. Diaz (2012), Constrained full-waveform inversion by model reparameterization, *Geophysics*, *77*(2), R117, doi:10.1190/geo2011-0196.1.

Hobbs, R., et al. (2007), GO geophysical oceanography: A new tool to understand the thermal structure and dynamics of oceans, D318 Cruise report, Durham Univ., Durham, U. K.

Hobbs, R. W., D. Klaeschen, V. Sallarès, E. Vsemirnova, and C. Papenberg (2009), Effect of seismic source bandwidth on reflection sections to image water structure, *Geophys. Res. Lett.*, *36*, L00D08, doi:10.1029/2009GL040215.

Holbrook, W. S. (2003), Thermohaline fine structure in an oceanographic front from seismic reflection profiling, *Science*, *301*(5634), 821–824, doi:10.1126/science.1085116.

Holbrook, W. S., and I. Fer (2005), Ocean internal wave spectra inferred from seismic reflection transects, *Geophys. Res. Lett.*, *32*, L15604, doi:10.1029/2005GL023733.

Huang, X. H., H. B. Song, M. P. Luis, and Y. Bai (2011), Ocean temperature and salinity distributions inverted from combined reflection seismic and XBT data, *Chin. J. Geophys.*, *54*(3), 307–314.

Jiménez Tejero, C., D. Dagnino, V. Sallarès, and C. R. Ranero (2015), Comparative study of objective functions to overcome noise and bandwidth limitations in full waveform inversion, *Geophys. J. Int.*, *203*(1), 632–645, doi:10.1093/gji/ggv288.

Kennett, B., and N. J. Kerry (1979), Seismic waves in a stratified half space, *Geophys. J. R. Astron. Soc.*, *57*(3), 557–583, doi:10.1111/j.1365-246X.1979.tb06779.x.

Köhn, D., D. De Nil, A. Kurzmann, A. Przebindowska, and T. Bohlen (2012), On the influence of model parametrization in elastic full waveform tomography, *Geophys. J. Int.*, *191*(1), 325–345, doi:10.1111/j.1365-246X.2012.05633.x.

Kormann, J., B. Biescas, N. Korta, J. de la Puente, and V. Sallarès (2011), Application of acoustic full waveform inversion to retrieve high-resolution temperature and salinity profiles from synthetic seismic data, *J. Geophys. Res.*, *116*, C11039, doi:10.1029/2011JC007216.

Krahmann, G., P. Brandt, D. Klaeschen, and T. Reston (2008), Mid-depth internal wave energy off the Iberian Peninsula estimated from seismic reflection data, *J. Geophys. Res.*, *113*, C12016, doi:10.1029/2007JC004678.

Lailly, P. (1983), The seismic inverse problem as a sequence of before stack migrations, *Conference on Inverse Scattering, Theory and Applications,* Society for Industrial and Applied Mathematics, in edited by J. Bednar, et al., pp. 206–220, SIAM, Philadelphia, Penn.

Lambert, J. D. (1991), *Numerical Methods for Ordinary Differential Systems: The Initial Value Problem*, John Wiley, N. Y.

McDougall, T. J., and P. M. Barker (2011), Getting started with TOES-10 and the Gibbs Seawater (GSW) Oceanographic Toolbox, *SCOR/IAPSO WG127*, vol. 168, 28 pp., CSIRO Marine and Atmospheric Research, Hobart, Tasmania.

Mora, P. (1989), Inversion = migration + tomography, *Geophys.*, 54(12), pp. 1575–1586, Springer, doi:10.1190/1.1442625.

Mulder, W. a., and R. É. Plessix (2008), Exploring some issues in acoustic full waveform inversion, *Geophys. Prospect.*, *56*, 827–841, doi:10.1111/j.1365-2478.2008.00708.x.

Müller, P., J., McWilliams, and M. Molemaker (2005), Routes to dissipation in the ocean: The two-dimensional/three-dimensional turbulence conundrum, in edited by H. Z. Baumert, J. Simpson, and J. Sündermann, 652 pp., Marine Turbulence, Observations and Models, Results of the CARTUM Project, Cambridge Univ. Press, Cambridge, U. K.

Nocedal, J. (1980), Updating quasi-Newton matrices with limited storage, *Math. Comput.*, *35*(151), 773–773, doi:10.1090/S0025-5718-1980-0572855-7.

Nocedal, J., and J. W. Stephen (2006), *Numerical Optimization*, American Mathematical Society, Springer, Providence, Rhode Island, USA, doi:10.1007/978-0-387-40065-5.

Padhi, A., S. Mallick, W. Fortin, W. S. Holbrook, and T. M. Blacic (2015), 2-D ocean temperature and salinity images from pre-stack seismic waveform inversion methods: An example from the South China Sea, *Geophys. J. Int.*, *202*(2), 800–810, doi:10.1093/gji/ggv188.

Papenberg, C., D. Klaeschen, G. Krahmann, and R. W. Hobbs (2010), Ocean temperature and salinity inverted from combined hydrographic and seismic data, *Geophys. Res. Lett.*, *37*, L04601, doi:10.1029/2009GL042115.

Plessix, R. É., G. Baeten, J. W. de Maag, F. ten Kroode, and Z. Rujie (2012), Full waveform inversion and distance separated simultaneous sweeping: A study with a land seismic data set, *Geophys. Prospect.*, *60*(4), 733–747, doi:10.1111/j.1365-2478.2011.01036.x.

Pratt, R. G. (1999), Seismic waveform inversion in the frequency domain, Part 1: Theory and verification in a physical scale model, *Geophysics*, *64*(3), 888, doi:10.1190/1.1444597.

Ravaut, C., S. Operto, L. Improta, J. Virieux, a. Herrero, and P. Dell'Aversana (2004), Multiscale imaging of complex structures from multifold wide-aperture seismic data by frequency-domain full-waveform tomography: Application to a thrust belt, *Geophys. J. Int.*, *159*(3), 1032–1056, doi:10.1111/j.1365-246X.2004.02442.x.

Richardson, P. L., A. S. Bower, and W. Zenk (2000), A census of Meddies tracked by floats, *Prog. Oceanogr.*, *45*(2), 209–250, doi:10.1016/S0079-6611(99)00053-1.

Ruddick, B. (2003), Oceans. Sounding out ocean fine structure, *Science*, *301*(5634), 772–773, doi:10.1126/science.1086924.

Sallarès, V., B. Biescas, G. Buffett, R. Carbonell, J. J. Dañobeitia, and J. L. Pelegrí (2009), Relative contribution of temperature and salinity to ocean acoustic reflectivity, *Geophys. Res. Lett.*, *36*, L00D06, doi:10.1029/2009GL040187.

Sallarès, V., J. F. Mojica, B. Biescas, D. Klaeschen, and E. Gràcia (2016), Characterization of the sub-mesoscale energy cascade in the Alboran Sea thermocline from spectral analysis of high-resolution MCS data, *Geophys. Res. Lett.*, *43*, doi:10.1002/2016GL069782.

Sheen, K. L., N. J. White, and R. W. Hobbs (2009), Estimating mixing rates from seismic images of oceanic structure, *Geophys. Res. Lett.*, *36*, L00D04, doi:10.1029/2009GL040106.

Shuey, R. (1985), A simplification of the Zoeppritz equations, *Geophysics*, *50*(4), 609–614.

Song, H., L. M. Pinheiro, B. Ruddick, and F. C. Teixeira (2011), Meddy, spiral arms, and mixing mechanisms viewed by seismic imaging in the Tagus Abyssal Plain (SW Iberia), *J. Mar. Res.*, *69*(4), 827–842, doi:10.1357/002224011799849309.

Stockwell, J. W. (1997), Free software in education: A case study of CWP/SU: Seismic Unix, *Leading Edge*, *16*, 1045–1049.

Tait, R. I., and M. R. Howe (1968), Some observations of thermo-haline stratification in the deep ocean, *Deep Sea Res. Oceanogr. Abstr.*, *15*, 275–280.

Tarantola, A. (1984), Inversion of seismic reflection data in the acoustic approximation, *Geophys.*, *49*(8), 1259–1266. doi:10.1190/1.1441754.

Thorpe, S. (2005), *The Turbulent Ocean*, 437 pp., Cambridge Univ. Press, Cambridge, U. K.

Virieux, J., and S. Operto (2009), An overview of full-waveform inversion in exploration geophysics, *Geophysics*, *74*(6), WCC1–WCC26, doi:10.1190/1.3238367.

Wood, W. T., W. S. Holbrook, M. K. Sen, and P. L. Stoffa (2008), Full waveform inversion of reflection seismic data for ocean temperature profiles, *Geophys. Res. Lett.*, *35*, L04608, doi:10.1029/2007GL032359.

Zhang, W., and X. Chen (2006), Traction image method for irregular free surface boundaries in finite difference seismic wave simulation, *Geophys. J. Int.*, *167*(1), 337–353, doi:10.1111/j.1365-246X.2006.03113.x.

Zhang, W., and Y. Shen (2010), Unsplit complex frequency-shifted PML implementation using auxiliary differential equations for seismic wave modeling, *Geophysics*, *75*(4), T141–T154, doi:10.1190/1.3463431.